

PHYSICAL REVIEW C

NUCLEAR PHYSICS

THIRD SERIES, VOLUME 37, NUMBER 2

FEBRUARY 1988

Breakup-fusion analysis of continuum spectra of α - and h-induced reactions

T. Udagawa, X. -H. Li,* and T. Tamura

Department of Physics, University of Texas, Austin, Texas 78712

(Received 20 April 1987)

Calculations are performed for the continuum spectra of protons, deuterons, and tritons emitted from α - and h-induced reactions of the breakup type. It is shown that the sum of the elastic breakup and breakup-fusion contributions fit the major parts of the observed spectra, except for the (α, p) case, where the theory underestimates experiment. It is then shown that the contributions from the quasi-elastic channel, in which $T=1$ dinucleons are created, account for most of the remaining (α, p) cross section. The quasi-elastic breakup and breakup-fusion are further shown to nicely fit two-proton coincidence data. The question of radial regions where the various modes of reactions dominantly occur is clarified, making it possible to understand why the various modes of reactions explain certain portions of the observed spectra.

I. INTRODUCTION

As is well known, the multistep direct reaction (MSDR) theory has been successful in analyzing a variety of data from reactions induced by both light and heavy ions. Earlier, the theory was applied exclusively to reactions that lead to discrete final states.¹ More recently, the theory has been extended to analyze continuum reaction data.²⁻⁴

Regarding the continuum reactions, however, there are cases which call for methods of descriptions that go beyond those developed in Refs. 2-4. In fact, evidence has been accumulated to indicate that there are reactions in which the direct and compound mechanisms play interwoven roles. These are reactions that have been called by many different names: inelastic breakup,⁵ absorptive breakup,⁶ incomplete fusion,⁷ massive transfer,⁸ or breakup-fusion (BF) (Ref. 9) reactions.

Take as an example the (α, p) reaction.¹⁰⁻¹² The forward peaked angular distribution of the continuum protons indicates that they were produced via a direct reaction. However, the coincidence measurement of these protons with γ rays demonstrates that the whole or a part of the rest of the system, i.e., the triton, fuses into the target to form a compound system. Similar features have been seen in many other reactions.⁶⁻¹³ The purpose of the present paper is to study BF reactions induced by α and h particles.

We have already reported¹⁴⁻¹⁷ on a few realistic calculations of the BF reactions. In these calculations, however, we have included only the elastic BF (EBF), i.e., the fusion that takes place via the elastic breakup (EB) channel, where the broken-up pair and also the tar-

get are all in their ground states. However, particles like α and h have a large spectroscopic amplitude for breaking up into quasi-elastic (QE) breakup channels, in which one or both of the broken-up pair are in their excited states. For instance, the α particle can break up strongly into $d^* + d^*$ and $2p + 2n$, where d^* , $2p$, and $2n$ denote $T=1$ di-nucleon systems. In this paper, we shall study, along with EB and EBF, the breakup of the projectile into these QE channels and the fusion that takes place in these channels. We shall call the breakup into the QE channels the quasi-elastic breakup (QEB) and the (partial) fusion taking place in these channels the quasi-elastic BF (QEBF).

We have presented^{18,19} the formalism of the EB and EBF calculations, and in Sec. II A, we summarize the formulas thus obtained. In Sec. II B, we then formulate the calculations of QEB and QEBF, which are new in this paper. In Sec. III, we discuss the details of the numerical calculations, because this was not done in either Refs. 18 or 19, in spite of the fact that our use of the finite range method requires it. In Sec. IV, results of numerical calculations are presented and are compared with experimental data. We consider not only the singles cross section, but also some of the coincidence cross sections. A further discussion of the results obtained in Sec. IV is presented in Sec. V, explaining in particular the significance of using the finite range method in our calculation. Section VI concludes this paper.

II. CROSS SECTION FORMULAS

A. Elastic BF cross sections

We first consider the elastic BF (EBF) reaction, which may be written symbolically as

$$a + A \rightarrow b + x + A \rightarrow b + B^* . \quad (2.1)$$

The two steps (i.e., the two arrows) in (2.1) stand, respectively, for the breakup of the projectile a into $b + x$, and the subsequent fusion of x into the target A to form B^* . Note that we are considering here the simplest possible BF process, in that we treat the first step as a simple elastic breakup (EB). The second step of the process is the fusion (absorption) of x into A (to form B^*), the particle b being a spectator in this step.

Let us call the systems consisting of $a + A$, $b + B$, and $x + A$ as a , b , and x channels, respectively, and also denote the optical model distorted wave functions for the relative motions in these channels as $\chi_a^{(+)}$, $\chi_b^{(-)}$, and $\chi_x^{(-)}$, respectively. $\chi_i^{(\pm)}$ ($i = a, b$, and x) satisfies the following Schrödinger equation:

$$(E_i - T_i - U_i)\chi_i^{(\pm)} = 0 , \quad (2.2)$$

where E_i , T_i , and U_i are, respectively, the energy, the kinetic energy, and the (optical) potential in the channel i . We ignore in the present work the spin orbit term in U_i . Also, we assume that the spin of the target is zero.

The EBF cross section may then be given as^{18,19}

$$\frac{d^2\sigma^{\text{BF}}}{dE_b d\Omega_b} = (2\pi/\hbar w_a)\rho(E_b) \frac{1}{(2s_a + 1)} \times \sum_{m_x m_b m_a} [\langle \psi_x^{(+)} | W_x | \psi_x^{(+)} \rangle / \pi] , \quad (2.3)$$

where $\rho(E_b)$ is the phase space volume of the emitted particle b , and s_a is the spin of a . The summation indices m_a , m_b , and m_x are the projections of spins of the particles a , b , and x , respectively. In addition, $\psi_x^{(+)}$ is the wave function in the x channel defined as

$$| \psi_x^{(+)} \rangle = G_x^{(+)} \rho_x , \quad (2.4)$$

where

$$\frac{d^2\sigma^{\text{EB}}}{dE_b d\Omega_b} = (2\pi/\hbar w_a)\rho(E_b)\rho(E_x) \frac{1}{(2s_a + 1)} \sum_{m_x m_b m_a} | \langle \chi_b^{(-)} \chi_x^{(-)} \varphi_b \varphi_x \varphi_A | V_a | \chi_a^{(+)} \varphi_a \varphi_A \rangle |^2 , \quad (2.9)$$

where $\rho(E_x)$ is the phase space volume of x . The rest of the notation has been explained above.

B. Quasi-elastic BF cross sections

Similarly as in (2.1), the quasi-elastic BF (QEBF) process may be written as

$$a + A \rightarrow c + x + A \rightarrow c + C^* \rightarrow b + y + C^* . \quad (2.10)$$

The first two steps in (2.10) are the same as those in (2.1), except that the very first step is a QEB process. Namely, c is left in a (metastable) excited state. The third step in (2.10) describes the eventual separation of c into $b + y$, where b is the particle that is to be observed.

The QEB processes that we consider explicitly in Sec. IV are the following four:

$$\rho_x = \langle \chi_b^{(-)} \varphi_b \varphi_x \varphi_A | V_a | \chi_a^{(+)} \varphi_a \varphi_A \rangle , \quad (2.5)$$

$$G_x^{(+)} = 1/(E_x - T_x - U_x + i\varepsilon) , \quad (2.6)$$

with

$$V_a = U_x + U_b - U_a , \quad (2.7)$$

$$E_x = E_a - E_b + Q_3 . \quad (2.8)$$

In Eq. (2.5), the symbol $(|| \rangle)$ is used to mean that the integration is taken over all the coordinates except the x -channel coordinate \mathbf{r}_x , while φ_i ($i = a, b, x$, and A) are intrinsic wave functions of the particle i . Clearly, the m_i dependence of the matrix element in (2.3) comes from that of φ_i . In (2.8), Q_3 stands for the Q value of the three-body breakup reaction.

As seen in (2.4) and (2.5), $\psi_x^{(+)}$ depends on $\chi_b^{(-)}$. Since $\chi_b^{(-)}$ depends on E_b and Ω_b , so does $\psi_x^{(+)}$. This dependence of $\psi_x^{(+)}$ on E_b and Ω_b is the origin of the dependence of the right-hand side of (2.3) on E_b and Ω_b .

It should be remarked that Eq. (2.3) contains contributions not only from true fusion but also from other (direct) reactions that take place in the x channel (i.e., between x and A). If the contribution from the true fusion process is to be singled out, W_x^F has to be replaced by a fusion potential W_x^F , where W_x^F is the part of W_x that is responsible for the true fusion.²⁰ In the calculations to be reported in Sec. IV, we use W_x^F instead of W_x because we are concerned with the b -singles cross sections. If we are to fit cross sections of (a, bxn) type reactions (obtained, e.g., from the b - γ coincidence measurements), we need to use W_x^F .

In the calculations in Sec. IV, contributions not only from EBF, but also from EB are included. In the EB, x is emitted along with b . The cross section formula for the EB process is well known,⁵ but we give it here for completeness. It reads

$$\alpha + A \rightarrow 2p + 2n + A \rightarrow 2p + C^* \rightarrow p + p + C^* , \quad (2.11a)$$

$$\alpha + A \rightarrow d^* + d^* + A \rightarrow d^* + C^* \rightarrow p + n + C^* , \quad (2.11b)$$

$$h + A \rightarrow 2p + n + A \rightarrow 2p + C^* \rightarrow p + p + C^* , \quad (2.11c)$$

$$h + A \rightarrow d^* + p + A \rightarrow d^* + C^* \rightarrow p + n + C^* . \quad (2.11d)$$

In all of the processes in (2.11), the $T = 1$ di-nucleons, d^* , $2p$, and $2n$ are produced in the first step QEB.

The contribution to the b -singles cross section from QEB and QEBF may then be given as

$$\frac{d^2\sigma_b^{\text{QE}}}{dE_b d\Omega_b} = \int dE_y d\Omega_y J \frac{d^4\sigma}{dE_c d\Omega_c d\varepsilon d\omega} , \quad (2.12a)$$

where

$$\frac{d^4\sigma}{dE_c d\Omega_c d\varepsilon d\omega} = \frac{d^2\sigma}{dE_c d\Omega_c} \frac{d^2W}{d\varepsilon d\omega} \quad (2.12b)$$

and

$$\frac{d^2\sigma}{dE_c d\Omega_c} = \frac{d^2\sigma^{\text{QEB}}}{dE_c d\Omega_c} + \frac{d^2\sigma^{\text{QEBF}}}{dE_c d\Omega_c} \quad (2.12c)$$

In (2.12a), ε denotes the internal energy, which c carries, while ω denotes the direction of the relative motion between b and y . J is the Jacobian for the coordinate transformation from the set $(E_c \Omega_c \varepsilon \omega)$ to $(E_b \Omega_b E_y \Omega_y)$, E_i and Ω_i ($i=b, c$, and y) denoting the energy and the direction of motion of the particle i . As seen in (2.12b), the quadruple differential cross section $d^4\sigma/dE_c d\Omega_c d\varepsilon d\omega$ is given as a product of two factors. The second factor $d^2W/d\varepsilon d\omega$ may be called the spectroscopic strength function for the QEB process in which a breaks up into c and x . The former factor $d^2\sigma/dE_c d\Omega_c$ is the c -singles cross sections and is given by (2.12c) as a sum of QEB and QEBF cross sections, which are denoted, respectively, by $d^2\sigma^{\text{QEB}}/dE_c d\Omega_c$ and $d^2\sigma^{\text{QEBF}}/dE_c d\Omega_c$. These two cross sections have the same form as the EB and EBF cross sections had in (2.9) and (2.3), respectively.

The spectroscopic strength function $d^2W/d\varepsilon d\omega$ may in principle be obtained in terms of the Fourier transform of the internal wave function φ_{by} in the cluster c , i.e., as

$$\frac{d^2W}{d\varepsilon d\omega} = \rho(\varepsilon) |\varphi_c(\mathbf{k})|^2, \quad (2.13a)$$

where

$$\varphi_c(\mathbf{k}) = \int e^{i\mathbf{k}\mathbf{r}} \varphi_{by}(r) d^3r \quad (2.13b)$$

However, φ_{by} is not well known for the purpose of the present paper to describe QEB processes. In the numerical calculations performed in Sec. IV, we do not use (2.13), but parametrize $d^2W/d\varepsilon d\omega$. This parametrization will be discussed in Eq. (4.1) in Sec. IV.

In addition to the contributions of the QEB and

QEBF processes to the b -singles cross section, as given by (2.12a), we also calculate the angular correlation between b and y . It is given by

$$\frac{d^2\sigma^{\text{QE}}}{d\Omega_b d\Omega_y} = \int dE_b dE_y J \frac{d^4\sigma}{dE_c d\Omega_c d\varepsilon d\omega} \quad (2.14)$$

III. DETAILS OF THE BF CALCULATIONS

In Sec. II, we presented cross section formulas for the EBF and QEBF reactions. In the present section, we discuss details on how to carry out the numerical calculations. We shall concentrate on the BF cross section of (2.3), because the prescription given for this case can also be used for the evaluation of the BF part of the QEBF cross section of (2.12).

A. Simplification due to the absence of the spin-orbit interaction

Throughout this paper we ignore (as also done before^{18,19}) the spin-orbit interactions; these interactions are insignificant for the continuum cross sections. The important merit of doing this is that we can completely dissociate the calculation of the overlap integral of the intrinsic wave functions from that of the distorted waves. The overlap integral in question is then given as

$$\begin{aligned} \langle \varphi_x \varphi_b | \varphi_a \rangle &= \sum_{sl_2} C_{s_a s_b s_x l_2 s}^{(2)} \langle s_b m_b s m_s | s_a m_a \rangle \\ &\quad \times \langle l_2 m_2 s_x m_x | s m_s \rangle \varphi_{l_2 m_2}(\mathbf{r}_2), \end{aligned} \quad (3.1)$$

where $C_{s_a s_b s_x l_2 s}^{(2)}$ is the spectroscopic amplitude,²¹ while $\varphi_{l_2 m_2}(\mathbf{r}_2)$ is the wave function for the relative motion between x and b . The orbital angular momentum and its z component for this motion are denoted, respectively, by l_2 and m_2 . $\langle jmj'm' | j''m'' \rangle$ is the Clebsch-Gordan coefficient.

We now introduce the special part x -channel wave function, and its partial expansion as

$$\begin{aligned} \psi_{x;l_2 m_2}^{(+)}(\mathbf{r}_x) &= G_x^{(+)}(\chi_b^{(-)} | V_a | \chi_a^{(+)} \varphi_{l_2 m_2} \rangle \\ &= (1/r_x) \sum_{l_x m_x} (-)^{m_2} \langle l_x m_x l_2 - m_2 | l m_l \rangle u_{l_x l_2 l m_l}(r_x) i^{l_x} Y_{l_x m_x}(\Omega_x). \end{aligned} \quad (3.2)$$

The radial partial wave function $u_{l_x l_2 l m_l}(r_x)$ is then found to satisfy

$$[(\hbar^2/2\mu_x)(d^2/dr_x^2 - l_x(l_x+1)/r_x^2) + E_x - U_x] u_{l_x l_2 l m_l}(r_x) = \rho_{l_x l_2 l m_l}(r_x), \quad (3.3)$$

with

$$\rho_{l_x l_2 l m_l}(r_x) = \sum_{m_x m_2} (-1)^{m_2} \langle l_x m_x l_2 - m_2 | l m_l \rangle r_x (i^{l_x} Y_{l_x m_x} \chi_b^{(-)} | V_a | \chi_a^{(+)} \varphi_{l_2 m_2} \rangle. \quad (3.4)$$

Equation (3.3) is to be solved so that $u_{l_x l_2 l m_l}(r_x)$ satisfies the following outgoing boundary condition

$$u_{l_x l_2 l m_l}(r_x) \rightarrow \exp(i\sigma_{l_x}) S_{l_x l_2 l m_l}(G_{l_x} + iF_{l_x}). \quad (3.5)$$

In (3.5), F_{l_x} and G_{l_x} are the regular and irregular Coulomb wave functions, respectively, while σ_{l_x} is the Coulomb

phase shift. $S_{l_x l_2 l m_l}$ is the S matrix for the EB reaction.

Inserting (3.1) and (3.2) into (2.3), the BF cross section is written, in the partial wave expanded form, as

$$\frac{d^2\sigma^{\text{BF}}}{dE_b d\Omega_b} = (2\pi/\hbar v_a) \rho(E_b) \sum_{sl_2} |C_{s_a s_b s_x l_2 s}^{(2)}|^2 \frac{1}{(2l_2+1)} \sum_{l_x l m_l} (\langle u_{l_x l_2 l m_l} | W_x | u_{l_x l_2 l m_l} \rangle / \pi). \quad (3.6)$$

An important remark is in order here. The cross section formula (3.6) describes not only the b -singles cross section, but also the probability with which the compound nucleus B^* with a given pair of spin I and its z component M is populated. (Note that $I=l$ and $M=m_l$.) Since E_b is uniquely related to the energy E^* of the compound nucleus, the above probability of population is in fact obtained as a function of E^* , as well as of I and M .

The EB cross section can be written in terms of the source function $\rho_{l_x l_2 l m_l}$, and of χ_{l_x} defined in Eq. (39b), as

$$\frac{d^2\sigma^{\text{EB}}}{dE_b d\Omega_b} = (2\pi/\hbar v_a) \rho(E_b) \rho(E_x) \sum_{sl_2} |C_{s_a s_b s_x l_2 s}^{(2)}|^2 \frac{1}{(2l_2+1)} \sum_{l_x l m_l} |(4\pi/k_x) \int \chi_{l_x}(r_x) \rho_{l_x l_2 l m_l}(r_x) dr_x|^2. \quad (3.7)$$

This cross section can also be written in terms of the $S_{l_x l_2 l m_l}$ introduced in (3.5), because

$$\int \chi_{l_x} \rho_{l_x l_2 l m_l} dr_x = -\frac{2\mu_x}{\hbar^2 k_x} \exp(i\sigma_{l_x}) S_{l_x l_2 l m_l}. \quad (3.8)$$

B. Source functions

The most decisive quantity that appears in (3.6) is the wave function $u_{l_x l_2 l m_l}$. It can be obtained easily by solving (3.3), once the source function $\rho_{l_x l_2 l m_l}$ is known. This source function $\rho_{l_x l_2 l m_l}$ is closely related to the DWBA (transition) amplitude of the first-step breakup process. In fact, if $\rho_{l_x l_2 l m_l}$ is multiplied by the x -channel distorted wave, and then integrated over the coordinate r_x , the result is nothing but the usual DWBA amplitude for EB. [This fact is seen in (3.7).] As is well known, this DWBA amplitude involves a six-dimensional integral. This means that the construction of $\rho_{l_x l_2 l m_l}$ in-

volves a five-dimensional integral.

It is remarkable that the evaluation of this five-dimensional integral is more involved than that of the six-dimensional integral (which is well known in the usual exact-finite-range (EFR) DWBA calculations²¹). The reason is that $\rho_{l_x l_2 l m_l}$ has to be obtained as a function of r_x , which forces one to transform one of the channel coordinates, r_a or r_b , into r_x . Namely, one has to perform a coordinate transformation so as to express the distorted wave [either $\chi_a^{(+)}(r_a)$ or $\chi_b^{(-)}(r_b)$] as a function of r_x . In the usual EFR-DWBA calculations, we need to perform a coordinate transformation for the bound state wave functions,²¹ however this is much simpler, if not trivial, than to transform the distorted wave function. (The number of bound state wave function is very limited, very often equals one, while there are a number of partial waves in the distorted wave.) In what follows, we explain how to perform this coordinate transformation and then to evaluate the five-dimensional integral.

We first perform the partial wave expansion of the distorted waves $\chi_a^{(+)}$ and $\chi_b^{(-)*}$

$$\chi_a^{(+)}(r_a, \mathbf{k}_a) = \frac{4\pi}{k_a r_a} \sum_{l_a m_a} i^{l_a} \chi_{l_a}(k_a, r_a) Y_{l_a m_a}(\hat{r}_a) Y_{l_a m_a}^*(\hat{\mathbf{k}}_a), \quad (3.9a)$$

$$\chi_b^{(-)*}(r_b, \mathbf{k}_b) = \frac{4\pi}{k_b r_b} \sum_{l_b m_b} i^{l_b} \chi_{l_b}(k_b, r_b) Y_{l_b m_b}(\hat{r}_b) Y_{l_b m_b}^*(-\hat{\mathbf{k}}_b). \quad (3.9b)$$

We also give here $\varphi_{l_2 m_2}$ somewhat more explicitly as

$$\varphi_{l_2 m_2}(r_2) = i^{l_2} [\chi_{l_2}(r_2)/r_2] Y_{l_2 m_2}(\hat{r}_2). \quad (3.9c)$$

Inserting (3.9) into (3.4), we see that the latter is rewritten [defining $\omega_l(r) = \chi_l(r)/r$ and $\hat{l} = \sqrt{2l+1}$] as

$$\begin{aligned} \rho_{l_x l_2 l m_l}(r_x) = & \frac{4\pi\sqrt{4\pi}}{k_a k_b} r_x \sum_{l_a l_b} \langle l_a 0 l_b m_l | l m_l \rangle \hat{l}_a Y_{l_a m_a}^*(\hat{\mathbf{k}}_b) i^{l_a - l_b + l_2 - l_x} \\ & \times \hat{l}^{-1} \int d\mathbf{r}_2 d\hat{\mathbf{r}}_x V_a \omega_{l_2}(r_2) \omega_{l_a}(r_a) \omega_{l_b}(r_b) [(Y_{l_x} Y_{l_2})_l (Y_{l_a} Y_{l_b})_l]_{00}. \end{aligned} \quad (3.10)$$

In (3.10) there appear four radial coordinate vectors, r_2 , r_x , r_a , and r_b . They are, however, related through the following relations:

$$\begin{aligned} \mathbf{r}_2 &= \alpha(\mathbf{r}_a - \mathbf{r}_x), \\ \mathbf{r}_b &= \alpha\mathbf{r}_a - \frac{x(a+A)}{Bb}\mathbf{r}_x \quad \text{with } \alpha \equiv \frac{a}{b}. \end{aligned} \quad (3.11)$$

Therefore, we have only two independent vectors, and we choose them to be \mathbf{r}_a and \mathbf{r}_x . The integration is then to be carried out over \mathbf{r}_a and the angle part ($\hat{\mathbf{r}}_x$) of \mathbf{r}_x .

In carrying out the integration over the angles, we use the same technique as used before.²² Namely, we make use of the fact that the integrand is a scalar and therefore does not depend on the choice of the coordinate system. We choose as the z axis the direction of \mathbf{r}_a , as the x axis the direction that is orthogonal to the z axis and lies in a plane defined by \mathbf{r}_a and \mathbf{r}_x ; this is illustrated in Fig. 1. Then, we see that Eq. (3.10) can be reduced to the two dimensional integral given as

$$\begin{aligned} \rho_{l_x l_2 l m_l}(r_x) &= \frac{4\pi\sqrt{4\pi}}{k_a k_b} r_x \sum_{l_a l_b} \langle l_a 0 l_b m_l | l m_l \rangle \hat{l}_a Y_{l_b m_l}^*(\hat{\mathbf{k}}_b) i^{l_a - l_b + l_2 - l_x} \hat{l}_x^{-2} \hat{l}_a \hat{l}_b \hat{l}_x \hat{l}_2 \\ &\quad \times \sum_{m'_1 m'_2} \langle l_a 0 l_b m'_1 | l m'_1 \rangle \langle l_x m'_1 l_2 m'_2 | l m'_1 \rangle (\alpha^3/2) \\ &\quad \times \int r_a^2 dr_a \omega_{l_a}(r_a) \int d\mu_x \bar{P}_{l_x m'_1}^*(\mu_x) V_a \omega_{l_2}(r_2) \omega_{l_b}(r_b) \bar{P}_{l_2 m'_2}^*(\mu_2) \bar{P}_{l_b m'_1}(\mu_b), \end{aligned} \quad (3.12)$$

where μ_i and \bar{P}_{lm} are defined as

$$\mu_i = \cos\vartheta_i \quad (i=2, x, \text{ and } b), \quad (3.13a)$$

$$\bar{P}_{lm} \equiv \frac{\sqrt{4\pi}}{2l+1} Y_{lm}(\vartheta, 0). \quad (3.13b)$$

In all the calculations we performed so far, we assumed $l_2=0$, an assumption that is valid for light-ion induced reactions. Under this restriction, l becomes equal to l_x and the source function is greatly simplified. It takes the final form given as

$$\begin{aligned} \rho_{l_x m_x}(r_x) &= \frac{4\pi\sqrt{4\pi}}{k_a k_b} r_x \sum_{l_a l_b} \langle l_a 0 l_b m_x | l_x m_x \rangle \hat{l}_a Y_{l_b m_x}^*(\hat{\mathbf{k}}_b) i^{l_a - l_b - l_x} \hat{l}_a \hat{l}_b \hat{l}_x^{-1} \\ &\quad \times \sum_{m'_x} \langle l_a 0 l_b m'_x | l_x m'_x \rangle (\alpha^3/2) \int r_a^2 dr_a \omega_{l_a}(r_a) \int d\mu_x \bar{P}_{l_x m'_x}^*(\mu_x) V_a \omega_{l_2}(r_2) \omega_{l_b}(r_b) \bar{P}_{l_b m'_x}(\mu_b). \end{aligned} \quad (3.14)$$

We also note here that we use V_a given as

$$V_a = U_x + U_b - U_a. \quad (3.15)$$

This is a choice normally made in the EFR-DWBA calculations for stripping type reactions.

As we remarked above, the calculation of $\rho_{l_x m_x}$ is the most involved, and in order to speed up this calculation, we used a variety of techniques which were developed in the past for the EFR-DWBA calculations.^{1,21} This helped us to minimize computational time. The rather large amount of numerical results we present in Sec. IV will testify to the efficiency of our calculations.

IV. NUMERICAL RESULTS AND COMPARISON WITH EXPERIMENT

We now present results of the numerical calculations performed for the EB, EBF, QEB, and QEBF reactions, and compare them with experiment. The calculations were done for the $^{58}\text{Ni}(\alpha, p)$, (α, d) , and (α, t) reactions with the incident energies of $E_\alpha = 80$ and 160 MeV,²³ the

$^{90}\text{Zr}(\alpha, p)$ and $(\alpha, 2p)$ reactions with $E_\alpha = 140$ MeV,^{24,25} and the $^{165}\text{Ho}(h, p)$ and (h, d) reactions with $E_h = 100$ MeV.²⁶ This means that the calculations were performed with both strongly bound (α) and loosely bound (h) projectiles, and for both the massive transfer type $[(\alpha, p)$ and $(h, p)]$, and light particle transfer type $[(\alpha, d)$, (α, t) , and $(h, d)]$ reactions. [Actually the (α, d) reaction is neither massive nor light-particle transfer reaction. We, nevertheless, classify it as a light-particle transfer type reaction, for the reason to be explained below.] Because we have treated a wide variety of cases in this manner, we feel we now have a good overall view of the mechanism of the breakup reactions. In what follows, we first explain the choice of the parameters involved in the calculations, and then present the results.

A. Choice of parameters

The most important parameters involved in the calculations are the optical potential parameters. They were mostly taken from the literature: Those for α , h , and t

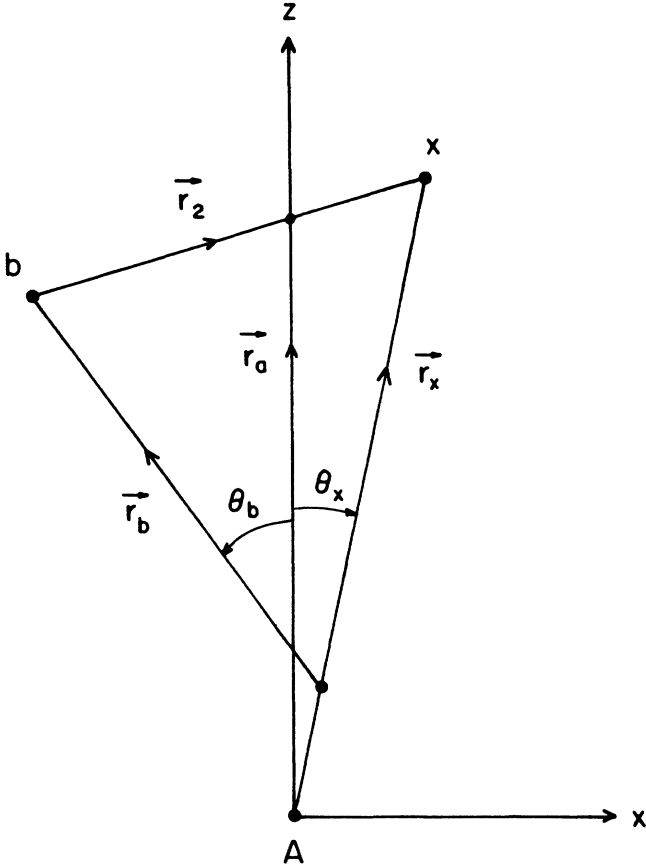


FIG. 1. Coordinates relevant in the evaluation of the integral that appears in Eq. (3.16).

were taken from Shepard *et al.*,²⁷ for d from Daehnick, Childs, and Vrcelj,²⁸ and for p for $E_p < 20$ MeV, $E_p = 20-40$ MeV, and $E_p > 40$ MeV from Perey-Perey,²⁹ Becchetti-Greenlees,³⁰ and Menet *et al.*,³¹ respectively. The parameters for the $T=1$ di-nucleon systems are not known. We thus simply assumed them to be the same as those for d.

We may note here that the magnitude of the theoretical cross sections obtained depend to some extent on the choice of the optical model parameters. We nevertheless found that different choices of the parameters did not cause the change by more than a factor of 2. In other words, no dramatic dependence on parameters, as experienced in the DWBA calculations³² of the (α, p) reactions that lead to discrete final states, has been observed in the BF cross section calculations.

The spectroscopic factors used were $|C^{(2)}|^2 = 2$ for the (α, p) and (α, t) reactions, $= 3$ for the (α, d) reactions, $= 1$ for the (α, d^*) and $(\alpha, 2p)$ reactions, $= \frac{3}{2}$ for the (h, p) and (d, h) reactions, $= 1$ for the (h, d^*) reaction, and $= \frac{1}{2}$ for the $(h, 2p)$ reaction. The bound state wave function $u_{l_2}(r_2)$ (with $l_2=0$) was generated by using a Woods-Saxon potential with the geometry of $r_0=1.20$ fm and $a_0=0.67$ fm. The depth of the potential was determined by the well-known separation energy method. For the

$d^* + d^*$ and $2p + 2n$ systems, the separation energy was assumed to be equal to the binding energy of the α particle. A similar assumption was also made for the $2p + n$ and $d^* + p$ systems; the separation energies of these systems were set equal to the binding energy of h. This is equivalent to assuming that the intrinsic energy of the $T=1$ di-nucleon system is zero.

With the parameters and prescriptions as described above, the calculations of the EBF cross sections can now be executed. In calculating the contributions from the QEBF reactions, however, we need to know the spectroscopic strength function. [See Eq. (2.12).] As mentioned in Sec. II B, we parametrize the spectroscopic strength function, instead of making a calculation. We choose it as

$$\frac{d^2W}{d\varepsilon d\omega} = ne^{-\lambda\varepsilon}, \quad (4.1)$$

where n is fixed from the normalization condition that

$$\int d\varepsilon d\omega \frac{d^2W}{d\varepsilon d\omega} = 1. \quad (4.2)$$

The parameter λ in (4.1) is then treated as adjustable. Crudely speaking, $1/\lambda$ represents the correlation energy of the $T=1$ di-nucleon system in α or in h. The fact that this system has no bound state suggests that the correlation energy is small. In the present calculations, we simply chose $\lambda=0.5$. This value corresponds to a correlation energy of 2 MeV.

As seen in (2.12a) and (2.14), the evaluation of the contributions from QEB and QEBF requires one to carry out the integration over E_y and Ω_y , and over E_b and Ω_b , respectively. In either case, we need to know the values of $d^2\sigma/dE_c d\Omega_c$ at a large number of pairs of the E_c and Ω_c values. To calculate the cross sections for many pairs of these values is extremely time consuming. However, we again find that the cross section is a rather smooth function of E_c and Ω_c [$=(\vartheta_c, \varphi_c)$] so that it can be well represented by an analytic function. We found that $d^2\sigma/dE_c d\Omega_c$ can be written as

$$\frac{d^2\sigma}{dE_c d\Omega_c} = Ne^{-\alpha(P_c - P_0)^2} e^{-\beta\vartheta_c}, \quad (4.3)$$

where P_c is the momentum of c . The constants N , α , P_0 , and β were fixed by calculating the left-hand side of (4.3) for a very limited number of representative pairs of E_c and Ω_c . The values of these parameters calculated in this way for the $(\alpha, 2p)$ and $(h, 2p)$ reactions are listed in Table I. We used the same parameters also for the (α, d^*) and (h, d^*) reactions.

B. α -induced reactions

1. $^{58}\text{Ni}(\alpha, x)$ reaction

We start with the $^{58}\text{Ni}(\alpha, x)$ reactions, and present in Fig. 2 the energy spectra at $\vartheta_{\text{lab}}=6^\circ$ and in Figs. 3 and 4 the angular distributions. The theoretical cross sections σ^{th} , represented by solid lines in Figs. 2-4, include all possible contributions, i.e., those from EB and EBF for

TABLE I. Values of parameters that appear in Eq. (4.3).

	E (MeV)	N (mb/MeV sr)	α (1/amu MeV)	P_0 [(amu MeV) $^{1/2}$]	β
^{58}Ni	160	20.53	0.0941	19.0	0.121
	80	6.66	0.188	13.8	0.0792
^{90}Zr	140	13.44	0.110	17.9	0.140
^{165}Ho	100	50.9	0.211	17.8	0.159

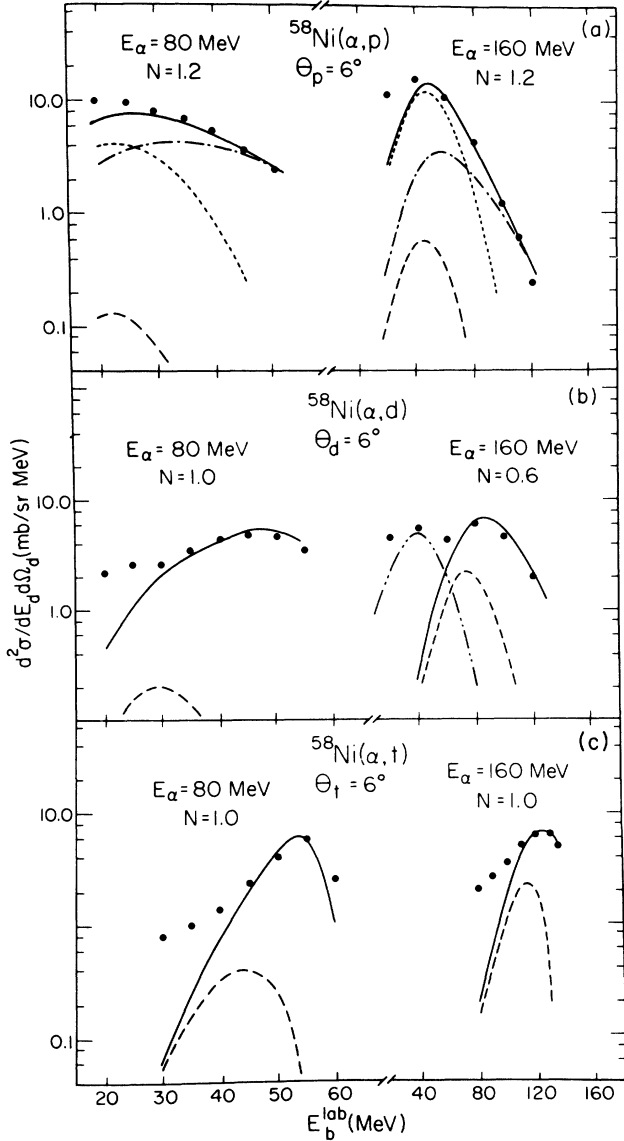


FIG. 2. Experimental and calculated energy spectra of (a) the $^{58}\text{Ni}(\alpha,p)$, (b) the $^{58}\text{Ni}(\alpha,d)$, and (c) the $^{58}\text{Ni}(\alpha,t)$ reactions with $E_\alpha = 80$ and 160 MeV. The data were taken from Ref. 23. The solid lines represent the sum of all the contributions, while the dashed lines represent σ^{EB} only. Also, the dashed-dotted and dotted lines shown in (a) represent σ^E and σ^{QE} , respectively, while the dashed-double-dotted line shown in (b) represents the contribution from the breakup-pickup and breakup-pickup-fusion reactions (Ref. 32).

the (α,d) and (α,t) reactions, and from EB, EBF, QEB, and QEBF for the (α,p) reactions. We shall denote the contributions from EB, EBF, QEB, and QEBF by σ^{EB} , σ^{EBF} , σ^{QEB} , and σ^{QEBF} , respectively. We shall also define σ^E and σ^{QE} as $\sigma^E = \sigma^{\text{EB}} + \sigma^{\text{EBF}}$ and $\sigma^{\text{QE}} = \sigma^{\text{QEB}} + \sigma^{\text{QEBF}}$. In Figs. 2–4, we presented σ^{EB} , σ^E , and σ^{QE} separately by the dashed, dashed-dotted, and dotted lines, respectively. In plotting these cross sections in these figures, an overall normalization factor N was multiplied into the calculated values. The values of N used are all very close to 1. The experimental data σ^{exp} were taken from Ref. 23.

The calculated spectra σ^{th} , shown in Fig. 2, fit the data rather well for all the (α,p) , (α,d) , and (α,t) reactions. Note that in the light particle transfer (α,d) and (α,t) reactions, $\sigma^{\text{th}} = \sigma^E$, while $\sigma^{\text{th}} = \sigma^E + \sigma^{\text{QE}}$ in the (α,p) reaction. It is remarkable that in the former two reactions the (major parts of the) experimental cross sections are explained by σ^E alone, while this is not the case in the massive transfer (α,p) reactions. In the (α,p) case, σ^E fits the data only at very high E_p region. The data are not fit even at the peak region. This was one of the difficulties encountered in our previous analysis of the (α,p) reaction.¹⁶ As seen in Fig. 2, however, the major parts of the gap between σ^E and σ^{exp} are filled by σ^{QE} . Note that the gap between σ^E and σ^{exp} increases with increasing incident energy, and it is remarkable that this energy dependence is also well accounted for by our present calculations.

We remarked above that the data of the (α,t) and (α,d) reactions were well explained by σ^E alone. Discrepancies are, nevertheless, seen in the low energy regions, particularly in the case of the (α,d) reactions. Note that the experimental deuteron spectra have second peaks at energies of about $E_\alpha/4$. Since this is the energy which each nucleon has in the projectile, a possible mechanism to create these second peaks is conjectured to be the following. Namely, the breakup of the α particle into $p + t$ (or $n + h$), with p (or n) then picking up one n (or p) from the target; the t (or h) is then fused into the target. We have estimated the contributions of these breakup-pickup and breakup-pickup-fusion processes, and found that the second peaks are explained very well in this way.³³ (The result of the calculation done in Ref. 33 for $E_\alpha = 160$ MeV is presented in Fig. 2 by the dashed-double-dotted line. We remark, however, that a few simplifying assumptions were made in performing these calculations, making the level of sophistication of the calculations done in Ref. 33 somewhat lower than that in the present paper. Improvement of the work of

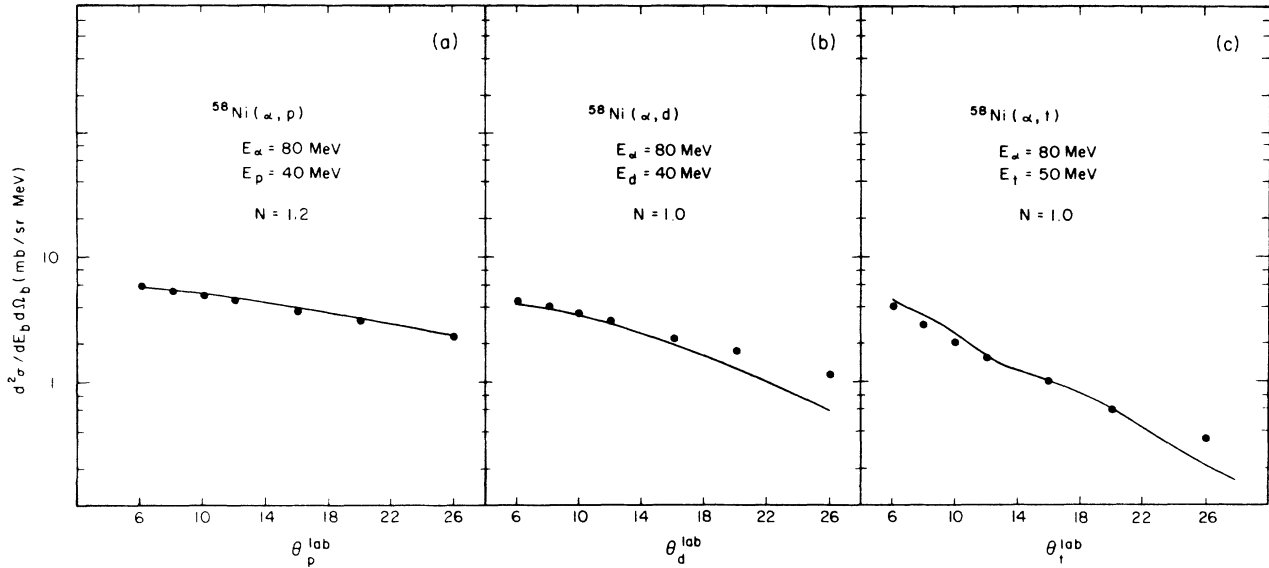


FIG. 3. Experimental and calculated angular distributions of (a) the $^{58}\text{Ni}(\alpha, p)$ reaction with $E_\alpha = 80$ MeV and $E_p = 40$ MeV, (b) the $^{58}\text{Ni}(\alpha, d)$ reaction with $E_\alpha = 80$ MeV and $E_d = 40$ MeV, and (c) the $^{58}\text{Ni}(\alpha, t)$ reaction with $E_\alpha = 80$ MeV and $E_t = 50$ MeV.

Ref. 33 is underway.)

We have plotted σ^{EB} separately in Fig. 2. As seen, it is rather small; the ratio $\sigma^{\text{EB}}/\sigma^{\text{EBF}}$ at the peak is roughly $\frac{1}{40}$, $\frac{1}{40}$, and $\frac{1}{10}$ for the (α, p) , (α, d) , and (α, t) reactions, respectively, for $E_\alpha = 80$ MeV. The ratio $\sigma^{\text{QEB}}/\sigma^{\text{QEBF}}$ is about the same as $\sigma^{\text{EB}}/\sigma^{\text{EBF}}$ for the (α, d) reaction. Note that σ^{EB} becomes relatively more important as b gets heavier, and also as E_α increases. Thus, for the (α, t) reaction at $E_\alpha = 160$ MeV, the σ^{EB} contribution is appreciable.

It is important to remark that the peaks of σ^{EBF} ap-

pear at energies which are (somewhat or very much) higher than are the peak energies of σ^{EB} . The peak energy of σ^{EB} is approximately equal to $E_0 = (b/a)E_\alpha$, i.e., the energy corresponding to the incident beam velocity. This means that the peak of σ^{EBF} shifts from E_0 to a higher energy, the amount of the shift increasing as b gets lighter. In Sec. V B, we explain why this happens.

The angular distributions given in Fig. 3 are for higher E_b , where the fits of σ^{th} to σ^{exp} are good, while those in Fig. 4 are for lower E_b , where $\sigma^{\text{th}} < \sigma^{\text{exp}}$. The fit of the angular distribution is very good in Fig. 3, but

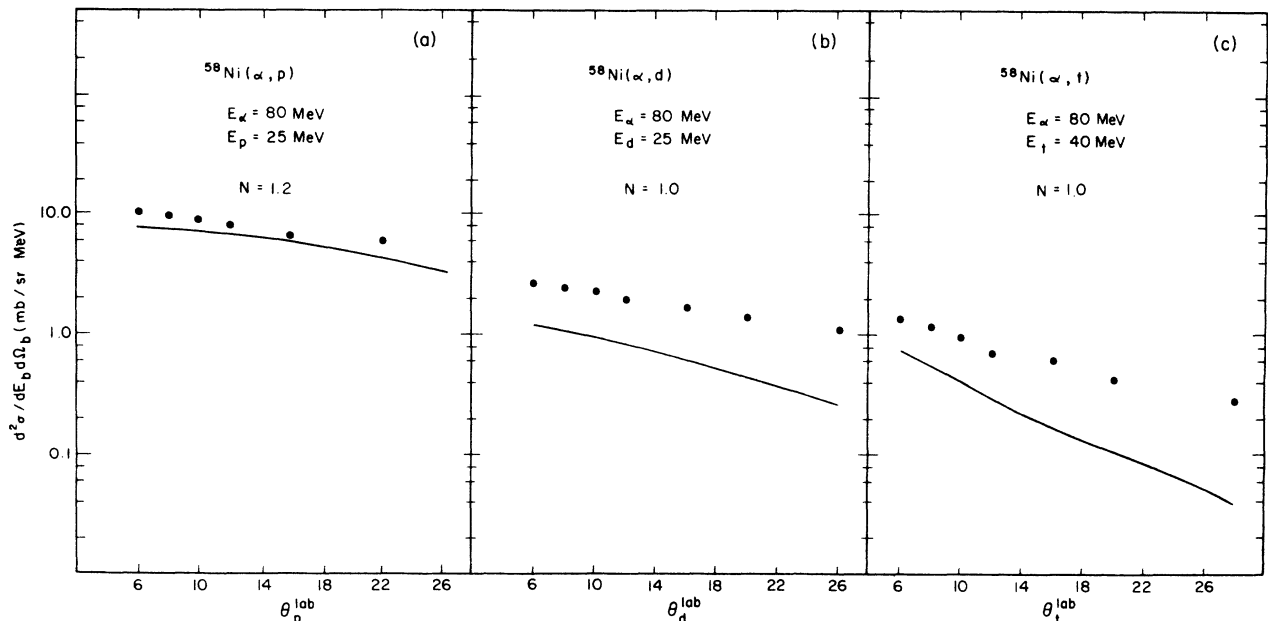


FIG. 4. Experimental and calculated angular distributions of (a) the $^{58}\text{Ni}(\alpha, p)$ reaction with $E_\alpha = 80$ MeV and $E_p = 25$ MeV, (b) the $^{58}\text{Ni}(\alpha, d)$ reaction with $E_\alpha = 80$ MeV and $E_d = 25$ MeV, and (c) the $^{58}\text{Ni}(\alpha, t)$ reaction with $E_\alpha = 80$ MeV and $E_t = 35$ MeV.

are poorer in Fig. 4, as expected. It is worthwhile to note that in Fig. 4, the difference between σ^{exp} and σ^{th} increases as the angle increases, suggesting that the yield at the backward angles comes from mechanisms that we have not yet taken into account.

2. $^{90}\text{Zr}(\alpha, x)$ reactions

In Fig. 5, we present the calculated p -singles cross sections of the $^{90}\text{Zr}(\alpha, p)$ reactions with $E_\alpha = 140$ MeV and compare them with the data.^{24,25} The meanings of the various theoretical curves are the same as those in Fig. 2. The closed circles are the measured p -singles cross section,²⁴ while the open circles are twice the contributions to the p -singles cross section deduced from the measured coincident $(\alpha, 2p)$ cross sections.²⁵ [The factor 2 was introduced in order to take into account the possible contribution from the (α, d^*) reactions. Also in deducing the contributions to the singles cross section, we assumed that the coincidence cross sections are independent of the azimuthal angle, an assumption that appears justified as argued in Ref. 25.] The σ^{th} are to be compared with the solid circles, while σ^{QE} with the open circles. In plotting the theoretical curves, we again introduced normalization factors: N for σ^{EB} and σ^{EBF} , and N' for σ^{QE} . The values of these factors are shown

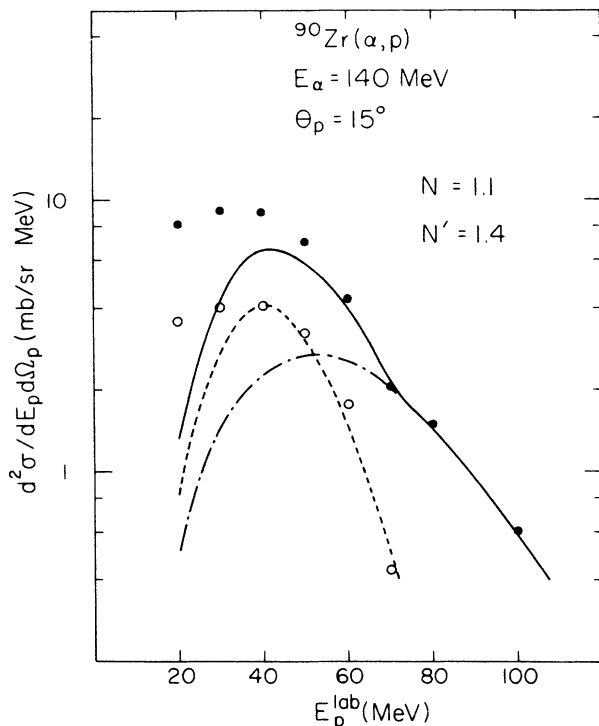


FIG. 5. Experimental and calculated energy spectra of the $^{90}\text{Zr}(\alpha, p)$ reaction with $E_\alpha = 140$ MeV. The closed and open circles are, respectively, the experimental singles cross section (Ref. 24) and twice the contribution from the coincident $(\alpha, 2p)$ reaction to the singles cross section (Ref. 25). The solid line represents the sum of all the contributions, while the dashed-dotted and dotted lines represent $(1.1 \times) \sigma^E$ and $(1.4 \times) \sigma^{\text{QE}}$, respectively.

in Fig. 5 and are very close to 1.

It is seen that the calculated σ^{th} and σ^{QE} both fit the data very well, except at very low energies. It is remarkable that we have achieved the fits not only of σ^{th} but also of σ^{QE} . This gives direct support of the validity of the calculations we made for the QEB and QEBF cross sections. The discrepancies in the low energy region may again be ascribed to higher order processes, including evaporation.

In Fig. 6, we present the calculated angular correlation cross section in the form of the angular distribution of the (second) proton measured in coincidence with the first proton measured at a fixed angle of $\vartheta_1 = 15^\circ$ (indicated by an arrow in the figure). The experimental data were taken from Ref. 25. An important feature of the measured angular distribution is that it is peaked at $\vartheta_2 \approx 0^\circ$ and is symmetric with respect to this peak angle, indicating that the two protons are very weakly correlated. It is remarkable that this characteristic feature is well reproduced by our calculation. The calculated angular distribution is peaked at $\vartheta_2 \approx 3^\circ$, which is indeed very close to 0° , and is almost symmetric with respect to this angle. In our calculation a rather small $1/\lambda$ value (2 MeV) was used, which corresponds to a rather weak correlation of two protons. Had a larger value, say, 5 MeV, been used, the resultant angular distribution would have peaked at $\vartheta_2 \approx 15^\circ$.

C. h-induced reactions

Calculations were done for the $^{165}\text{Ho}(h, p)$ and (h, d) reactions, with $E_h = 100$ MeV, corresponding to the exper-

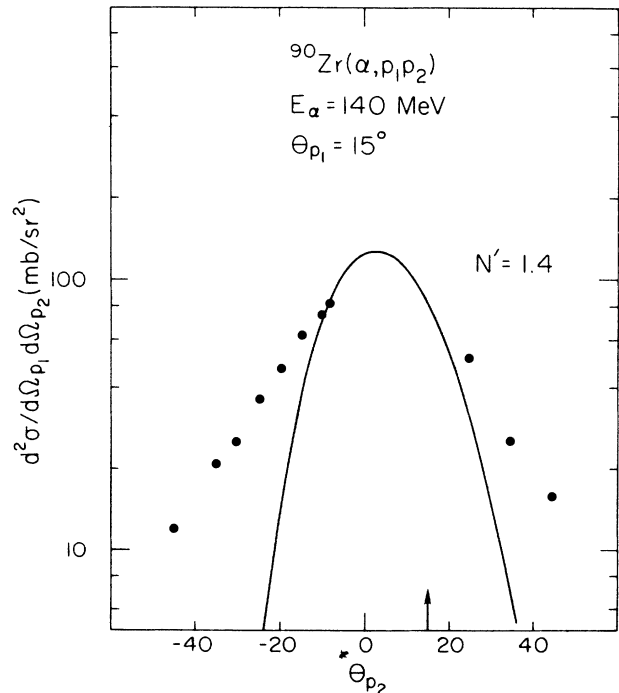


FIG. 6. Experimental and calculated angular correlation cross sections for the $^{90}\text{Zr}(\alpha, 2p)$ reaction with $E_\alpha = 140$ MeV. The data were taken from Ref. 25.

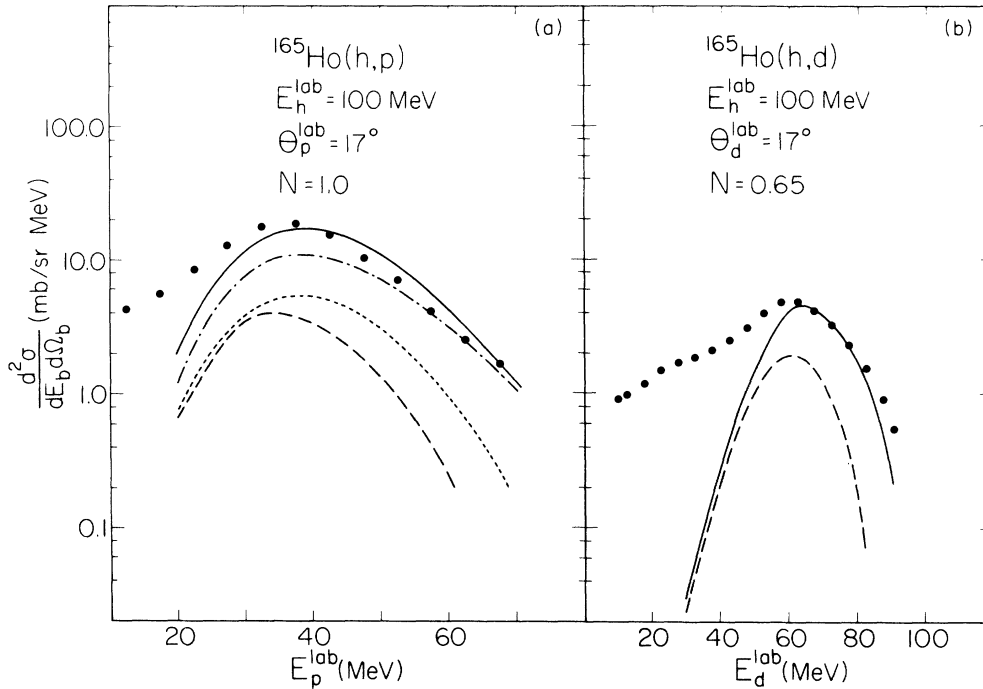


FIG. 7. Experimental and calculated energy spectra at $\vartheta_b^{\text{lab}} = 17^\circ$ of (a) the $^{165}\text{Ho}(h,p)$ and (b) the $^{165}\text{Ho}(h,d)$ reactions with $E_h^{\text{lab}} = 100$ MeV. The experimental data were taken from Ref. 31. The solid lines represent the sum of all the contributions, while the dashed lines represent σ^{EB} only. Also, the dashed-dotted and dotted lines shown in (a) represent σ^E and σ^{QE} , respectively.

iment done by Motobayashi *et al.*²⁶ In Ref. 26, data were taken not only of the singles cross sections, but also of the particle- γ and particle-particle coincidences. By using these coincidence data, the total (energy integrated) BF and EB cross sections were extracted. We can thus compare, in this case, the calculated total σ^{BF} and σ^{EB} separately to the data.

In Fig. 7, we present the calculated spectra and compare them with the data.²⁶ Again the overall normalization factor N was multiplied into each of the calculated cross sections. The values used were $N = 0.65$ for the (h,d) reaction, and $N = 1.0$ for the (h,p) reaction. The solid lines shown there include all possible contributions, i.e., EB and EBF for the (h,d) reaction and EB, EBF, QEB, and QEBF for the (h,p) reaction. On the other hand, the dashed, dashed-dotted, and dotted lines represent σ^{EB} , σ^E , and σ^{QE} , respectively. As seen, the calculated cross sections that include all the contributions fit the data rather well, except again at lower energies. In any case the general quality of the fit achieved here is very similar to that seen in the α -induced reactions.

Note that the discrepancy observed in the lower energies is somewhat larger in the (h,d) reaction than in the (h,p) reaction, and further that in the experimental spectrum of the (h,d) reaction, a second peak appears at around $E_d = 35$ MeV. This position is approximately equal to the incident energy per nucleon. Thus this situation is very similar to what has been seen in the (α ,d) reactions. As noted in Sec. IV B 1, this peak was explained³³ in terms of a simultaneous breakup-pickup and breakup-pickup fusion. We may thus expect that the

discrepancy seen in Fig. 5 will be largely removed, if calculations similar to those done in Ref. 33 are repeated.

In Table II, we list the energy integrated breakup (EB plus QEB) and BF (EBF plus QEBF) cross sections at $\vartheta = 17^\circ$, and compare them with the data.²⁶ The calculated cross sections fit the data fairly well, except that the calculated BF cross section for the (h,d) reaction is about half the experimental value. To have this discrepancy is not surprising, because we have underestimated the lower E_b part of the spectra (in Fig. 5).

It is worthwhile to note that the contributions from the EB (and QEB) reactions amount to 15–30% of the total singles cross sections. These figures are considerably larger than those in the α -induced reactions, which were 1–10%. This difference originates from the fact that h is more loosely bound than is α .

In Figs. 8 and 9, we compare the calculated angular distributions with experiment. Those in Fig. 8 are for higher E_b [$E_b = 60$ and 70 MeV for the (h,p) and (h,d) reactions, respectively], where the fit to the spectra was

TABLE II. Calculated and experimental energy integrated cross sections σ^{B} and σ^{BF} , respectively, for breakup and breakup-fusion modes, in the $^{165}\text{Ho}(h,p)$ and (h,d) reactions with $E_h = 100$ MeV. Data were taken from Ref. 26.

	(h,p)		(h,d)	
	Calc.	Exp.	Calc.	Exp.
σ^{BF} (mb/sr)	243	278	63	119
σ^{B} (mb/sr)	110	84	40	62

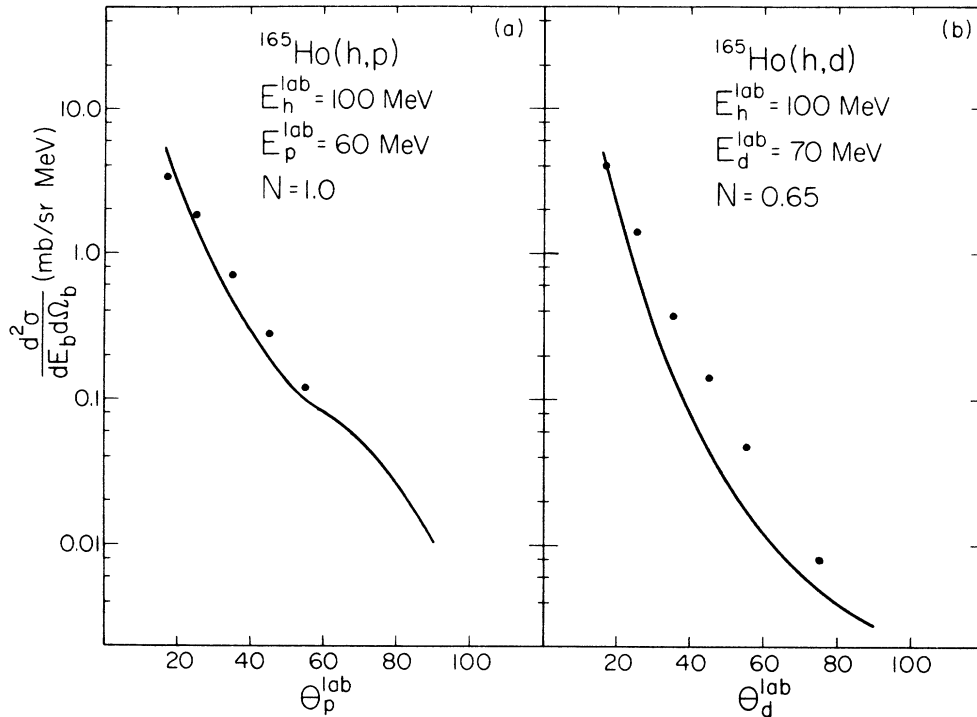


FIG. 8. Experimental and calculated angular distributions of (a) the $^{165}\text{Ho}(h,p)$ reaction with $E_h^{lab} = 100$ MeV and $E_p^{lab} = 60$ MeV, and (b) the $^{165}\text{Ho}(h,d)$ reaction with $E_h^{lab} = 100$ MeV and $E_d^{lab} = 70$ MeV.

good. On the other hand, those in Fig. 9 are for lower E_b ($E_b = 30$ and 60 MeV), where the fit to the spectra was poor. Thus, as expected, a much better fit to the data is seen in Fig. 8 than in Fig. 9.

V. DEEP PERIPHERAL NATURE OF BF REACTIONS

In this section, we study the radial region where the EB and EBF reactions take place dominantly. (The in-

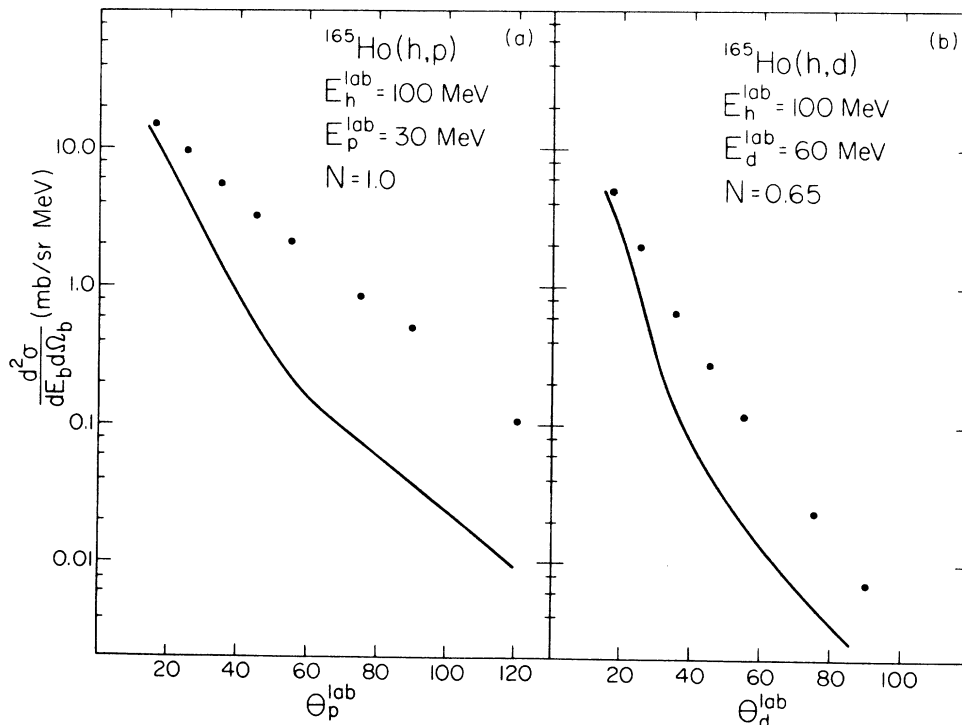


FIG. 9. Experimental and calculated angular distributions of (a) the $^{165}\text{Ho}(h,p)$ reaction with $E_h^{lab} = 100$ MeV and $E_p^{lab} = 30$ MeV, and (b) the $^{165}\text{Ho}(h,d)$ reaction with $E_h^{lab} = 100$ MeV and $E_d^{lab} = 60$ MeV.

formation obtained for these reactions apply also for the QEB and QEBF reactions.) More specifically we extract the values of three radii r_a , r_b , and r_x , which are, respectively, the radial positions, where the breakup of a , the emission of b , and the absorption (or emission) of x , tend to occur dominantly. Since they differ for EB and EBF, we are to obtain six radii r_c^i with $c=a, b$, and x and $i=EB$ and EBF.

A. Reaction regions

The r_c^i values are calculated as follows. We introduce lower (R_l) and upper (R_u) cutoff radii for the radial integrals, and calculate the EB and EBF cross sections as functions of these cutoff radii. [When R_l and R_u refer to r_a , these limits are used in the r_a integral in (3.14). When they refer to r_x , the integral that appears either in (3.6) or in (3.7) is used for this purpose. When R_l and R_u refer to r_b , we use again the integral in (3.14), interpreting it as a double integral that takes r_b and μ_x as integration variables.] The r_c^i value is then determined as the value of either R_l or R_u , where the cross section changes most rapidly. We can fix in this way two values of r_c^i , one from R_l and the other from R_u . In most of the cases studied these two values agreed with each other, enabling us to fix r_c^i uniquely. In cases where these two differed, we took their average as r_c^i .

The r_c^i values thus obtained are summarized in Tables III and IV, respectively, for the α - and h-induced reactions. In these tables, we also list values of the incident partial wave l_a^i that contributes most importantly to the reaction i ($=EB$ or EBF), and also the absolute value $|S_{l_a}^i|$ of the elastic scattering S -matrix corresponding to l_a^i .

We discuss first the results for the α -induced reactions. In Table III, we see that $r_a^{EB}=8.6, 8.2$, and 7.8 fm, respectively, for (α,p) , (α,d) , and (α,t) reactions. This means that the incident α breaks up in the peripheral region, irrespective of whether the particle b is p, d , or t , if this breakup is to result in pure EB. It is seen, however, that $r_a^{EBF}-r_a^{EB}=-1.8, -1.0$, and 0.0 fm for the above three reactions, meaning, in particular in the EBF-type (α,p) reaction, that the α particle penetrates deeper by 1.8 fm beyond the peripheral region before it is broken up. This feature which we may call the "deep-peripheral" nature (of the EBF reaction) is more remarkable when b is lighter (all but disappearing for $b=t$).

Table III also shows that r_b^i always takes a peripheral value (8.0–8.6 fm for all b and for both $i=EB$ and

EBF). This means that b is always emitted from the peripheral region, as it should be; otherwise it cannot escape. Similarly we see that $r_x^{EB}\simeq r_b^i$; this must again be the case.

We see, however, that $r_x^{EBF}<r_a^{EBF}$. This means that the absorption of x takes place in a region which is even deeper than where the breakup takes place. Note also that r_x^{EBF} decreases as x gets lighter. This is very natural, because the lighter x , the less absorptive it is, and thus it can penetrate deeper into the target before being absorbed.

The value of r_a^{EBF} describes the center of mass position of the a particle when its breakup occurs. It is then interesting to see whether we can relate r_a^{EBF} and r_b^{EBF} as

$$r_a^{EBF}=r_b^{EBF}-(x/a)\langle r_a \rangle, \quad (5.1)$$

where $\langle r_a \rangle$ is the size of the particle a . If we assume that $\langle r_a \rangle=2$ fm (which is somewhat larger than the means radius of the α particle), and take r_b^{EBF} from Table III, we see that Eq. (5.1) gives r_a^{EBF} as 6.5, 7.4, and 7.7 fm, respectively, for the (α,p) , (α,d) , and (α,t) reactions. These values are very close to 6.8, 7.2, and 7.8 fm, which are the corresponding values of r_a^{EBF} listed in Table III. This shows that (5.1) holds. The significance of (5.1) is that it gives a simple explanation on why the deep peripheral nature becomes more pronounced as x becomes heavier.

The values of l_a^i listed in Table III are seen to be roughly proportional to r_a^i . For the case of the (α,t) reaction, it takes the value of the grazing partial wave. For smaller b , however, l_a^{EBF} gets smaller, and thus gets strongly absorptive. (This fact is also seen in the smallness of $|S_{l_a}^i|$ in Table III.) Thus the EBF-type (α,p) reaction is induced by strongly absorptive (lower l) partial waves.

The results for the h-induced reactions shown in Table IV are more or less the same as those shown in Table III for the α -induced reactions. [The (h,p) and (h,d) reactions behave very similarly to the (α,d) and (α,t) reactions, respectively.] All the values of r_c^{EB} ($c=a, b$, and x) and r_b^{EBF} lie within a rather narrow range in the peripheral region. The strongest deep peripheral nature is seen in the (h,p) reaction which gives $r_a^{EBF}-r_a^{EB}=-0.6$ fm. Since this is much smaller (in magnitude) than $r_a^{EBF}-r_a^{EB}=-1.8$ fm encountered in the (α,p) case, we conclude that we do not see a very marked deep peripheral nature in the h induced reaction, as we did in the (α,p) case. We arrive at the same conclusion when we

TABLE III. The radii where the various α -induced reactions take place dominantly. The optimum value of the incident partial wave, and the absolute magnitudes of the corresponding elastic scattering S matrices are also given. These values are for the α -induced reactions.

Reaction	r_a^{EBF} (fm)	r_a^{EB} (fm)	r_x^{EBF} (fm)	r_x^{EB} (fm)	r_b^{EBF} (fm)	r_b^{EB} (fm)	$l_a^{EBF}(S)$	$l_a^{EB}(S)$
(α,p)	6.8	8.6	6.2	8.5	8.0	8.6	22(0.18)	26(0.80)
(α,d)	7.2	8.2	5.8	7.5	8.4	8.4	23(0.35)	25(0.70)
(α,t)	7.8	7.8	4.6	6.0	8.2	8.2	24(0.56)	24(0.56)

TABLE IV. Same as in Table III, except that the values are for h-induced reactions.

Reaction	r_h^{EBF} (fm)	r_h^{EB} (fm)	r_x^{EBF} (fm)	r_x^{EB} (fm)	r_b^{EBF} (fm)	r_b^{EB} (fm)	$l_h^{\text{EBF}}(S)$	$l_h^{\text{EB}}(S)$
(h,p)	9.3	9.9	7.8	9.5	10.3	10.3	29(0.5)	31(0.7)
(h,d)	9.8	9.9	8.7	9.5	10.3	9.8	29.5(0.5)	30(0.6)

look at the problem via l_a^i .

We may obtain a further insight into the EBF reaction mechanism by examining the x -channel partial wave function $u_{l_x m_x}$, and the source function $\rho_{l_x m_x}$; see Eqs. (3.3) and (3.14). In Fig. 10, we plotted the magnitudes and phases of $\rho_{l_x m_x}$ and $u_{l_x m_x}$ as functions of the radial distance r_x . [They are for $(l_x m_x) = (12, 0)$ in the (α, p) reaction with $E_a = 80$ MeV.] The $|\rho_{l_x m_x}|$ measures the strength with which x is produced, while $u_{l_x m_x}$ describes the propagation of the thus created x . [From now on we shall suppress the subscripts $(l_x m_x)$.]

It is seen that $|\rho|$ is peaked at $r_x = 6.1$ fm, which is very close to r_x^{EBF} given in Table III; this is expected. We also note that ρ has a phase that decreases with increasing r_x . This means that ρ has an incoming wave nature. The significance of this fact is that at the moment of its production, x has already a tendency to move towards the center of the target.

Reflecting the behavior of ρ , $|u|$ also has a large peak at $r_x \approx 6.3$ fm. It has also an incoming wave nature in the deep peripheral region. Note that u flips into an outgoing wave at the peripheral region, as it should. However, its magnitude here is extremely small. This means that the probability with which the particle x is emitted, along with b , is very small. This explains why $\sigma^{\text{EB}} \ll \sigma^{\text{EBF}}$.

In concluding this section, we want to emphasize that, in order to obtain all the results given above in this paper so far, it has been crucial that we have used an exact finite range description. Had the zero range approximation been used, all the positions r_a , r_b , and r_x would have coincided. Thus it is clear that the zero range description is incapable of describing properly, e.g., the different behaviors of the (α, p) and (α, t) reactions.

We may also remark that we showed earlier³⁴ that the zero-range calculations that include the finite-range corrections by means of the local energy approximation predicted very poorly the theoretical cross sections.

B. Angular momentum matching condition

As discussed in Sec. IV, the peak energies of the calculated σ^{EBF} for the (α, p) reaction were much higher than $E_0 = (b/a)E_a$, i.e., the energy that corresponds to the incident beam velocity. We showed in Ref. 16 that this shift of the peak was due to the deep peripheral nature of the reaction, which significantly affects the angular momentum matching condition. We shall briefly recapitulate here the argument of Ref. 16.

Let us first note that there are three angular momenta involved in the reaction. We denote by l_a^i , l_b^i , and l_x^i the

values of these angular momenta of partial waves that contribute most importantly for $i = \text{EB}$ or EBF . They depend on E_b , except that l_a^i is fixed once the incident energy is fixed. The matching condition which they satisfy may be given by

$$l_x^i = l_a^i - l_b^i \quad (\text{or } l_a^i = l_b^i + l_x^i). \quad (5.2)$$

To be more precise, this relation is to be satisfied only at a selected value of E_b^i of E_b , where the peak appears in the spectrum of b .

In order to see the way with which the condition (5.2) is satisfied, we plot in Fig. 11 l_x^i and $l_a^i - l_b^i$ for (a) $i = \text{EBF}$ and (b) $i = \text{EB}$ as functions of E_b . [We take here, as an example, the $^{58}\text{Ni}(\alpha, p)$ reaction with $E_a = 80$ MeV. Thus we have $a = \alpha$, $b = p$, and $x = t$.] The solid circles given in Fig. 11 were obtained by calculations

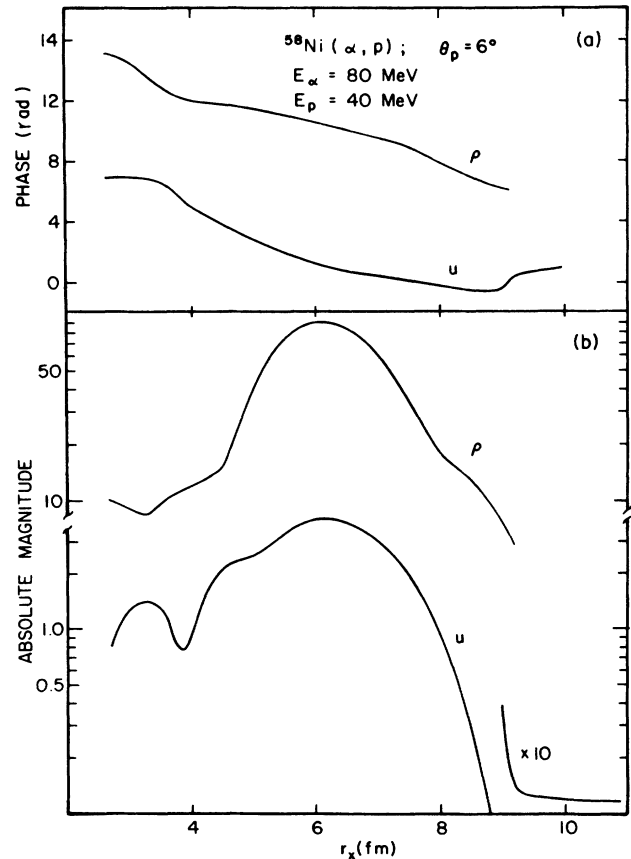


FIG. 10. Calculated phase and absolute magnitudes of the source function ρ_{lm} and the x -channel wave function u_{lm} for $(l, m) = (12, 0)$ for the (α, p) reaction with $E_a = 80$ MeV.

which used the upper and lower cutoff method, very similar to that used above for extracting r_c^i . On the other hand, the full and dashed lines drawn in the figure for l_x^i and l_b^i , respectively, were obtained by using the relations

$$l_c^i = R_c^i [2\mu_c(E_c - V_c^i)/\hbar^2]^{1/2} \quad (c = b \text{ and } x). \quad (5.3)$$

In calculating the l_c^i value from Eq. (5.3), we used $l_a^{\text{EB}} = 26$ and $l_a^{\text{EBF}} = 22$, listed in Table III. We also used $R_c^{\text{EB}} = 8.5$ fm and $V_c^{\text{EB}} = 4.4$ MeV for both $c = b$ and $c = x$, and $R_b^{\text{EBF}} = R_b^{\text{EB}}$, $V_b^{\text{EBF}} = V_b^{\text{EB}}$, $R_x^{\text{EBF}} = 6.5$ fm, and $V_x^{\text{EBF}} = -6.8$ MeV. All these R_c^i values are close to the r_c^i values tabulated in Table III. Also, the V_c^i values are the values of the potential energies evaluated at r_c^i . Since $r_x^{\text{EBF}} = 6.5$ fm is a deep peripheral value, we find that $V_x^{\text{EBF}} < 0$, showing that the nuclear potential is overwhelming the Coulomb potential here.

It is seen that, for the EB reaction, the two curves cross at $E_p = 20$ MeV, which is nothing but the beam velocity energy E_0 . The peak of σ^{EB} thus appears at this energy, which has been seen in Fig. 2(a). On the other hand, the crossing of the two curves for the EBF reaction occurs at $E_p = 40$ MeV, which is much higher than E_0 . The appearance of the peak of σ^{EBF} at $E_p = 40$ MeV, as seen in Fig. 2(a), is thus explained in this way.

Note that the above shift of the crossing point to higher E_b , when we switched from EB to EBF, has resulted essentially from the smallness of l_a^{EBF} as compared with l_a^{EB} . We can thus conclude that the shift occurred because of the deep peripheral nature of the EBF reaction.

The above result suggests that if the reaction is of a

peripheral nature, the peak will appear at an energy close to E_0 . This was indeed experienced in the (α, d) , (α, t) , (h, p) , and (h, d) reactions. Experimentally, we observe the peak appearing close to E_0 even in the (α, p) reaction. What we have shown in this paper is that this occurs, because the apparent (α, p) -type reaction is, in fact, dominated by the QE-type modes (α, d^*) and $(\alpha, 2p)$.

VI. CONCLUDING REMARKS

The breakup-fusion (BF) description has been applied to calculate continuum spectra of the α -induced (α, p) , (α, d) , and (α, t) and the h-induced (h, p) and (h, d) reactions. The quasi-elastic breakup (QEB) and the accompanying breakup-fusion (QEBF) reactions, along with the elastic breakup (EB) and elastic breakup-fusion (EBF), were also taken into account in the calculations. The results of these calculations were able to explain the major parts of the observed spectra for all the reactions considered, leaving unexplained only a small part of the spectra at the lower energy regions.

The results also showed that the dominant contributions came from the BF (EBF and QEBF) reactions and that the contributions from the simple breakup (EB and QEB) mechanisms were generally small, being less than 10% for the α -induced reaction, and 15–30% for the h-induced reactions. The increased importance of the latter for the h-induced reactions was attributed to the loosely bound nature of h. It was also observed that the relative importance of the simple breakup increased with increasing incident energy.

For the light ion transfer-type (α, d) , (α, t) , and (h, d) re-

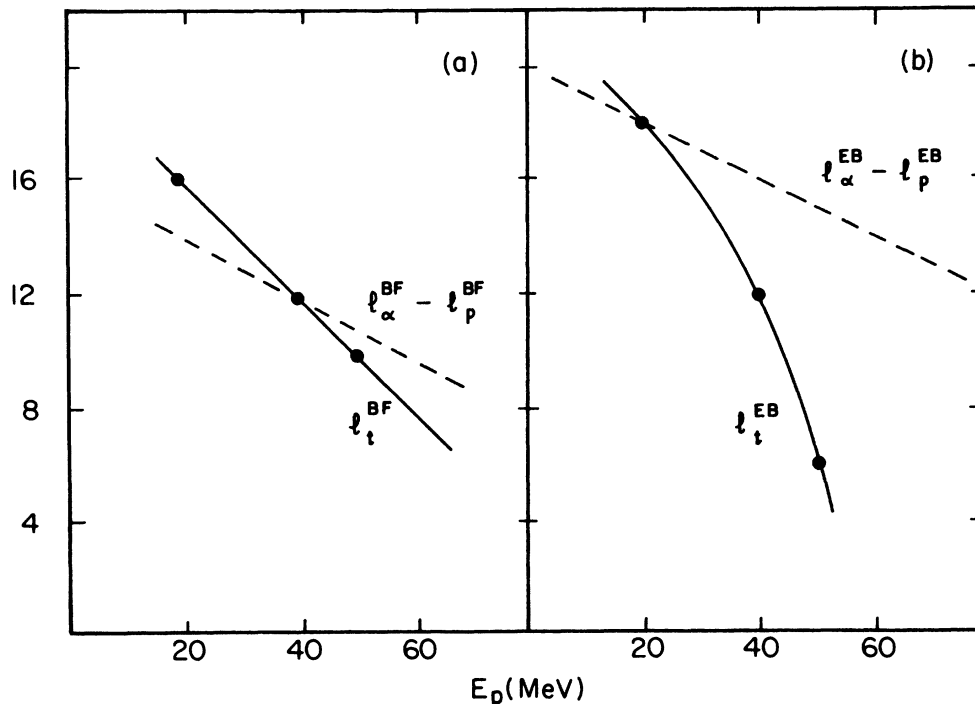


FIG. 11. Optimum angular momenta l_x^i and $l_a^i - l_b^i$ as functions of E_p , for the (a) EBF, and (b) EB. These are for the $^{58}\text{Ni}(\alpha, p)$ reaction with $E_\alpha = 80$ MeV.

actions, the contributions come only from the EBF and EB reactions, and these mechanisms alone were able to explain successfully the major parts of the observed spectra. For the massive transfer type (α, p) and (h, p) reactions, additional contributions come from QEBF and QEB, and it has been found that these additional contributions, particularly those from QEBF, were crucial in explaining the larger portion of the observed spectra. In fact, the contributions from the EBF and EB were able to explain only the spectra in the highest energy region.

The calculations of the QEBF and QEB reactions were further tested against the coincidence cross section data of the $^{90}\text{Zr}(\alpha, 2p)$ reaction with $E_\alpha = 140$ MeV. The results showed that the calculations fit the data rather well.

All these results permit us to conclude that our BF approach is working rather well, and thus can be regarded as a theory that is basically correct. It is particularly encouraging that we were able to explain the major parts of the spectra by taking into account the lowest order elastic and quasi-elastic breakup, and the following (partial) fusion. The remaining discrepancies in the lower energy region may certainly be ascribed to the next higher order processes. As such higher order processes, we may consider, e.g., the simultaneous breakup-pickup and breakup-pickup-fusion reactions. Very recently, we made an estimate of the contributions from these processes to the (α, d) reaction, showing that the second peak observed in the low energy region can in fact be explained by such a mechanism.³³

We also made a detailed study of the radial regions, where the breakup of the projectile, the emission of the outgoing particle, and the fusion of the rest of the broken-up pair take place dominantly. We found that in the massive transfer-type reactions, such as the (α, p) re-

actions, the breakup takes place within a deep peripheral region; a region which is considerably inside the usual peripheral region, and that the region where t is absorbed is still deeper. This deep peripheral nature, however, diminishes as the mass of the emitted particles increases. Thus, e.g., the (α, t) reaction takes place almost exclusively in the peripheral region.

We were also able to explain, from this deep peripheral nature, e.g., of the (α, p) reaction, why the peak of the EBF cross section for this reaction shifts to an energy much higher than the beam velocity energy. We may thus say that what we have achieved in this paper is not only to show that we can fit the data, but also to decipher the details of the mechanism of the reactions which we have dealt with here.

Extension of what we have done in this paper to heavy-ion-induced reactions is possible in principle, but very involved in practice. This is because a large number of channels are open in the heavy-ion case, and thus a huge amount of calculations are required. In one case, however, we have performed an analysis. It was a ($^{14}\text{N}, \alpha$) reaction in which we considered only the EB and EBF, where EB corresponded to the breakup of ^{14}N into α and ^{10}Be , ^{10}B , as well as α being assumed to stay in their ground states.¹⁴ Thus, although we were able to fit the data, the fit was limited to the highest energy part of the observed α -particle spectra. How to improve the situation by extending the fit to lower energies is now clear from what we have learned in the present study. It is necessary to include other breakup processes, e.g., the ($^{14}\text{N}, ^8\text{Be}$) reaction, which eventually give rise to lower energy α particles.

The present work was supported in part by the U.S. Department of Energy.

*Present address: Institute of Theoretical Physics, Peking University, Beijing, People's Republic of China.

¹N. Austern, *Direct Nuclear Reaction Theories* (Wiley, New York, 1970); G. R. Satchler, *Direct Nuclear Reactions* (Oxford, New York, 1984):

²T. Tamura, T. Udagawa, D. H. Feng, and K. K. Kan, *Phys. Lett.* **66B**, 109 (1977); T. Tamura and T. Udagawa, *ibid.* **78B**, 189 (1978); **71B**, 273 (1977); T. Tamura, H. Lenske, and T. Udagawa, *Phys. Rev. C* **23**, 2769 (1981); T. Udagawa and T. Tamura, in *Continuum Spectra in Heavy Ion Reactions*, edited by T. Tamura, J. B. Natowitz, and D. H. Youngblood (Harwood-Academic, New York, 1980), p. 155.

³H. Feshbach, A. K. Kerman, and S. E. Koonin, *Ann. Phys. (N.Y.)* **125**, 429 (1981).

⁴T. Tamura, T. Udagawa, and H. Lenske, *Phys. Rev. C* **26**, 379 (1982).

⁵B. Baur, F. Rösler, D. Trautmann, and R. Shyam, *Phys. Rep.* **111**, 333 (1984), and references therein.

⁶R. J. de Meijer and R. Kamermans, *Rev. Mod. Phys.* **57**, 147 (1985).

⁷T. Inamura, M. Ishihara, T. Fukuda, T. Shimoda, and H. Hirata, *Phys. Lett.* **68B**, 51 (1977); K. Siwek-Wilczynska, E. H. Du Marchie Van Voorthuysen, J. Van Popta, R. H.

Siemssen, and J. Wilczynski, *Phys. Rev. Lett.* **42**, 1599 (1979).

⁸D. R. Zolnowski, H. Yamada, S. E. Cala, A. C. Kahler, J. Pierce, and T. T. Sugihara, *Phys. Rev. Lett.* **41**, 92 (1978); T. Kishimoto and K. Kubo, in *Proceedings of the Symposium on High Spin Phenomena in Nuclei*, edited by T. L. Khoo, Argonne National Laboratory Report No. ANL-PHY-79-4, 1979, p. 535.

⁹T. Udagawa and T. Tamura, *Phys. Rev. Lett.* **45**, 1311 (1980).

¹⁰H. Ejiri, *Proceedings of International Conference on Nuclear Reaction Mechanisms*, Varenna, Italy, 1982 (unpublished).

¹¹R. M. Leider and B. Bochev, *Lecture Note, International School on Nuclear Physics, Neutron Physics and Nuclear Energy*, Varna, Bulgaria, 1981 (unpublished).

¹²B. Bochev, T. Kutsarova, R. M. Leidel, and T. Morek, *Nucl. Phys.* **A458**, 429 (1986).

¹³See, for instance, C. Gerschel, *Nucl. Phys.* **A387**, 297c (1982), and references therein.

¹⁴T. Udagawa, D. Price, and T. Tamura, *Phys. Lett.* **118B**, 45 (1982).

¹⁵T. Udagawa and T. Tamura, contribution to the International Conference on Nucleus-Nucleus Collisions, East Lansing, Michigan, 1982 (unpublished).

- ¹⁶T. Udagawa, X.-H. Li, and T. Tamura, *Phys. Lett.* **135B**, 333 (1984); **143B**, 15 (1984).
- ¹⁷X.-H. Li, T. Udagawa, and T. Tamura, *Phys. Rev. C* **30**, 1349 (1984).
- ¹⁸T. Udagawa and T. Tamura, *Phys. Rev. C* **24**, 1348 (1981).
- ¹⁹T. Udagawa and T. Tamura, *Phys. Rev. C* **33**, 494 (1986).
- ²⁰T. Udagawa, B. T. Kim, and T. Tamura, *Phys. Rev. C* **32**, 124 (1985).
- ²¹T. Tamura, *Phys. Rep.* **14**, 59 (1974).
- ²²T. Tamura, T. Udagawa, and H. Amakawa, *Prog. Theor. Phys.* **60**, 1238 (1978).
- ²³J. R. Wu *et al.*, *Phys. Rev. C* **19**, 659 (1979).
- ²⁴D. H. Holmgren, C. C. Chang, R. W. Koontz, and J. R. Wu, in *Proceedings of the Second International Conference on Nuclear Reaction Mechanisms*, June, 1979, Varenna, Italy (Cooperativa Libreria Universitaria Editrice Democratica, Milano, 1979), p. 35.
- ²⁵R. W. Koontz, Ph.D. thesis, University of Maryland, 1980 (unpublished).
- ²⁶T. Motobayashi *et al.*, *Nucl. Phys.* **A413**, 290 (1984).
- ²⁷J. R. Shepard *et al.*, *Nucl. Phys.* **A275**, 189 (1977).
- ²⁸W. W. Daehnick, J. D. Childs, and Z. Vrcelj, *Phys. Rev. C* **21**, 2253 (1980).
- ²⁹C. M. Perey and F. G. Perey, *Phys. Rev.* **132**, 755 (1963).
- ³⁰F. D. Becchetti, Jr. and G. W. Greenlees, *Phys. Rev.* **182**, 1190 (1969).
- ³¹J. J. H. Menet *et al.*, *Phys. Rev. C* **4**, 1114 (1971).
- ³²J. J. Hamill and P. D. Kunz, *Phys. Lett.* **129B**, 5 (1983).
- ³³X.-H. Li, T. Udagawa, and T. Tamura, *Phys. Lett.* **174B**, 1 (1986).
- ³⁴X.-H. Li, T. Udagawa, and T. Tamura, *Phys. Rev. C* **30**, 1895 (1985).